ADVANCED FUNCTIONAL MATERIALS
www.afm-journal.de

Efficiently Releasing the Trapped Energy Flow in White Organic Light-Emitting Diodes with Multifunctional Nanofunnel Arrays

*Lei Zhou, Qing-Dong Ou, Yan-Qing Li, Heng-Yang Xiang, Lu-Hai Xu, Jing-De Chen, Chi Li, Su Shen, Shuit-Tong Lee, and Jian-Xin Tang**

White organic light-emitting diodes (OLEDs) hold great promise for applications in displays and lighting due to high efficiency and superior white color balance. However, further improvement in efficiency remains a continuous and urgent demand due to limited energy flow extraction. A powerful method for drastically releasing the trapped energy flow in conventional white OLEDs is demonstrated by implementing unique quasi-periodic subwavelength nanofunnel arrays (NFAs) via soft nanoimprinting lithography, which is ideal for enhancing light extraction without any spectral distortion or angular dependence. The resulting efficiency is over 2 times that of a conventional OLED used as a comparison. The external quantum efficiency and power efficiency are raised to 32.4% and 56.9 lm W^{-1}, respectively. Besides, the substantial increase in efficiency over a broad bandwidth with angular color stability, the experimental proofs show that the NFA-based extraction structure affords the enticing capacity against scrubbing and the self-cleaning feature, which are critical to the commercial viability in practical applications.

1. Introduction

Organic light-emitting diodes (OLEDs) have attracted an enormous amount of attentions for applications in full-color flat-panel displays and solid-state lighting sources due to their enticing electrical, mechanical and optical features such as low power consumption, light weight, flexibility, fast response, high contrast, and wide viewing angle.[1–5] Along with significant efforts devoted to the development of high-performance phosphorescent or thermally activated delayed fluorescent emitters and novel device architectures, internal quantum efficiency has already achieved ≈100% for energy conversion due to the fully use of both singlet and triplet states.[6–8] Unfortunately, one of the major drawbacks of conventional OLEDs is the light confinement that a high fraction of energy flow generated in the emissive materials is trapped as substrate, waveguide (WG), and surface plasmon polariton (SPP) modes in glass substate, organic/transparent indium-tin-oxide (ITO) layers, and metallic rear electrode due to the mismatch of refractive indices in the flat multilayered structures.[9–11] Only 20%–30% energy flow can radiate outside the device as the useful light (denoted as leaky mode), which limits the development of highly efficient OLEDs. Accordingly, the efficient extraction of generated light provides the greatest potential for a substantial increase in external quantum efficiency (EQE) and power efficiency (PE) of OLEDs.

Indeed, various advanced light manipulation approaches have been extensively explored to facilitate the extraction of the confined photons by forming corrugated structures, such as microlens arrays,[12,13] modified substrates,[14,15] Bragg grating,[16,17] low-index dielectric grids,[18,19] photonic crystals,[20] antireflection coatings,[21] bioinspired deterministic aperiodic moth's eye nanostructures,[5,22] plasmonic nanocavity,[23] or periodic metallic grating electrode.[24,25] Nevertheless, it remains challenging for the light extraction in white OLEDs, since periodic structures often results in serious distortion of the emission spectra and/or the departure from ideal diffuse emission characteristics due to specific wavelength- or azimuthal angle-dependent outcoupling. To solve these drawbacks, strategies including the introduction of random scattering layer,[26] wrinkles,[27] nanopillar arrays,[28] or nanoislands,[29] have been proposed, but only experimentally demonstrated for monochromatic OLEDs. Therefore, a continuous and demanding task to further explore the novel light extraction nanostructure directly amenable to white OLEDs is urgently required.

Regardless of various nanostructures for efficient light extraction, it remains unclear whether nanoscale funnel-based

L. Zhou, Q.-D. Ou, Prof. Y.-Q. Li, H.-Y. Xiang, L.-H. Xu, J.-D. Chen, C. Li, Prof. S.-T. Lee, Prof. J.-X. Tang
Institute of Functional Nano & Soft Materials (FUNSOM)
Collaborative Innovation Center of Suzhou Nano Science and Technology
Jiangsu Key Laboratory for Carbon-Based Functional Materials & Devices
Soochow University
Suzhou 215123, China
E-mail: jxtang@suda.edu.cn
Dr. S. Shen
College of Physics Optoelectronics and Energy
Collaborative Innovation Center of Suzhou Nano Science and Technology
Soochow University
Suzhou 215006, China

DOI: 10.1002/adfm.201500310

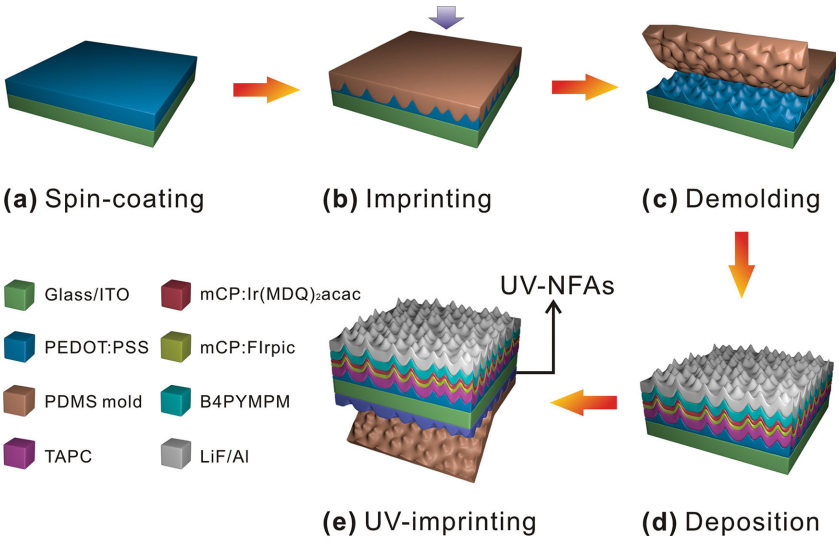

Figure 1. Schematic of the fabrication process of white OLEDs with dNFAs. a) Spin-coating the PEDOT:PSS layer on ITO-glass substrate. b) Imprinting the PEDOT:PSS layer by PDMS mold. c) Demolding the PDMS mold. d) Depositing the organic layers and metal electrode onto the patterned PEDOT:PSS. e) UV-imprinting the UV-curable resin on the glass substrate.

arrays (NFAs) or cone-based arrays (NCAs) are more beneficial to light extraction in white OLEDs. In addition to light extraction, other factors, such as ambient light absorption, contrast, image sharpness, low-glare, etc, are equally significant for display applications. Another important but usually neglected factor of the extraction structures is their mechanical property that has not been studied before. Particularly, the capability against scrubbing is a critical requirement in some practical applications, e.g., smart phones or touch screens.

To address the above-mentioned issues, we present the design, fabrication, simulation, and performance of an efficient method for releasing the trapped energy flow in white OLEDs. The broadband subwavelength NFAs have been implemented into organic layers and glass substrate simultaneously via soft nanoimprinting lithography (SNIL), which are ideal for enhancing light extraction without any spectral distortion or angular dependence. The resulting EQE of white OLEDs is improved to 29.4% at a luminance of 1000 cd m^{-2}, which is ≈2.3 times that of a control device with a flat architecture used as a comparison, and the maximum PE increases to 56.9 lm W^{-1}. Except for the excellent light extraction capability with superior angular color stability compared with that of NCAs, the experimental proofs reveal that the NFAs afford the enticing capacity against scrubbing and the self-cleaning feature, which are critical to the commercial viability in the practical applications.

2. Results and Discussion

2.1. Design and Fabrication of the NFAs

Figure 1 schematically illustrates the fabrication process of white OLEDs constructed with quasi-periodic NFAs by SNIL technique with the polydimethylsiloxane (PDMS) molds (see the details in Experimental Section).[22,30] The PDMS molds were fabricated using an anodized aluminum oxide template-assisted transfer and then multiple nanoimprinting lithography, etching, and mold duplication (see the details in Figures S1,S2, Supporting Information). A conductive polymer layer of poly (3,4-ethylenedioxy-thiophene) poly (styrenesulfonate) (PEDOT:PSS), which was spin-coated on ITO glass as a HIL, was inscribed to the NFAs (hereafter termed iNFAs) before the deposition of organic layers and metal electrode. On the contrary, the UV-curable resin drop-casted on glass surface was patterned with nanofunnel topography (hereafter termed eNFAs) by UV-assisted SNIL. For the device fabrication, the ITO glass substrates with both iNFAs and eNFAs (hereafter termed dNFAs) were produced by repeating the eNFAs after encapsulating the devices with a cap glass to prevent the damage to the formed iNFAs under pressure.

The surface morphologies of white OLEDs with NFAs were characterized by atomic force microscopy (AFM) and scanning electron microscopy (SEM), and displayed in **Figure 2**. The AFM image of the spin-coated PEDOT:PSS layer (Figure 2a) clearly

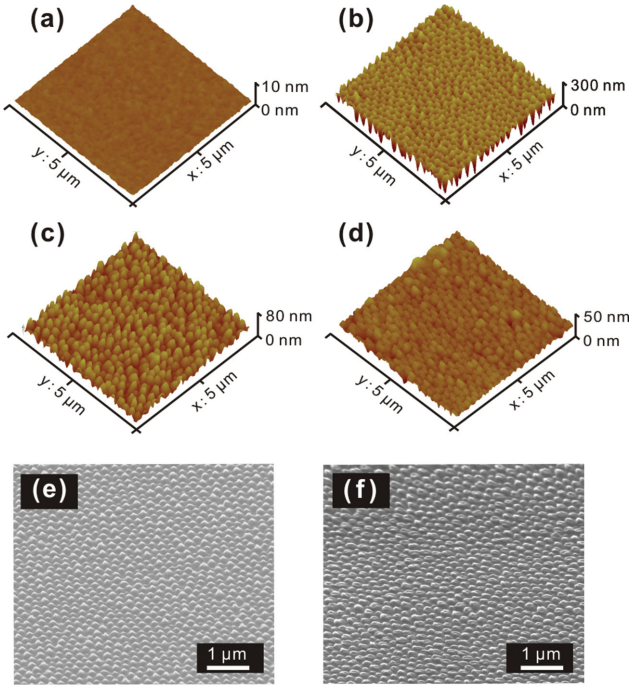

Figure 2. AFM images of a) flat PEDOT:PSS layer; b) patterned NFAs UV-resin on glass surface (period: ≈250 nm, groove depth: ≈250 nm, fill factor: ≈0.6); (c) patterned PEDOT:PSS layer on ITO-glass substrate (period: ≈250 nm, groove depth: ≈80 nm, and fill factor: ≈0.6); d) OLED with organic layers and Al cathode deposited on patterned PEDOT:PSS substrate (period: ≈250 nm, groove depth: ≈40 nm, and fill factor: ≈0.6). SEM images of e) patterned PEDOT:PSS layer on ITO-glass substrate and f) OLED with organic and Al cathode layers deposited on the patterned PEDOT:PSS are also shown for comparison.

reveals a rather smooth surface with a root-mean-square (RMS) roughness of approximately 1.1 ± 0.1 nm. In contrast, it is evident that the NFAs were successfully transferred onto the UV-resin and PEDOT:PSS surface (Figure 2b–d), exhibiting a continuously tapered morphology. Furthermore, Figure 2e,f shows the corresponding SEM images of the corrugated PEDOT:PSS layer before and after the subsequently deposited organic layers and metal electrode. It is apparent that each successive layer closely followed the surface profile of the corrugated PEDOT:PSS layer. The uniform well-defined eNFAs on UV-resin (Figure 2b), iNFAs on PEDOT:PSS (Figure 2c), and Al rear electrode (Figure 2d) show an almost identical period of ≈250 nm and a fill factor of ≈0.6, while their groove depths are ≈250, ≈80, and ≈40 nm, respectively. Here, a larger groove depth was used for imprinted UV-resin eNFAs to ensure a high aspect-ratio (≥1) for efficient enhancement of optical transmittance at the substrate/air interface,[31,32] while the smaller groove depth for PEDOT:PSS iNFAs is designed to suppress possible anomalies in current flow inside the OLED device.[33]

2.2. Optical and Mechanical Properties of NFAs

Figure 3 compares the optical and mechanical properties of various substrates without and with NFAs. As apparently shown in Figure 3a, the use of dNFAs on ITO-coated glass resulted in the highest enhancement of optical transmittance than the cases of only iNFAs or eNFAs, which was ≈6.8% larger than the bare substrate in the entire visible regime. Meanwhile, a lowest reflection value (≈5.7%) was realized for the substrate constructed with dNFAs (Figure 3b). A striking feature observed from the photograph in Figure 3b is that the coating of NFAs on ITO-coated glass substrate resulted in an excellent antireflection property, while the bare substrate shown a vivid reflection image. The significantly reduced reflection to ambient light is rather useful for improving the OLED's image contrast and glare property. According to the previous reports,[34,35] the improved optical features over the broadband spectrum is ascribed to the gradient refractive index distribution of NFAs at the interface. In addition, Figure 3c plots the angular dependence of the transmittance of various substrates at a fixed wavelength of 550 nm, revealing a significant improvement over a wide viewing angle for the use of NFAs. Especially, when the viewing angle is beyond the critical angle (41.8°) for glass substrates, the substrates using NFAs show a slower decrease in the optical transmittance, implying the capability of NFAs for extracting the trapped light from the WG and substrate modes more efficiently in a wider angle.

The robustness of NFAs was tested and shown in Figure 3d. As a comparison, the NCAs were produced by a negative mold with the same period, groove depth and fill factor. It is noted that the NFAs and NCAs exhibited the almost identical broadband antireflective effect (Figure S3, Supporting Information). Instead, the NFAs afford the striking capacity against scrubbing (e.g., only ≈8% decrease in transmittance after 200 scratching

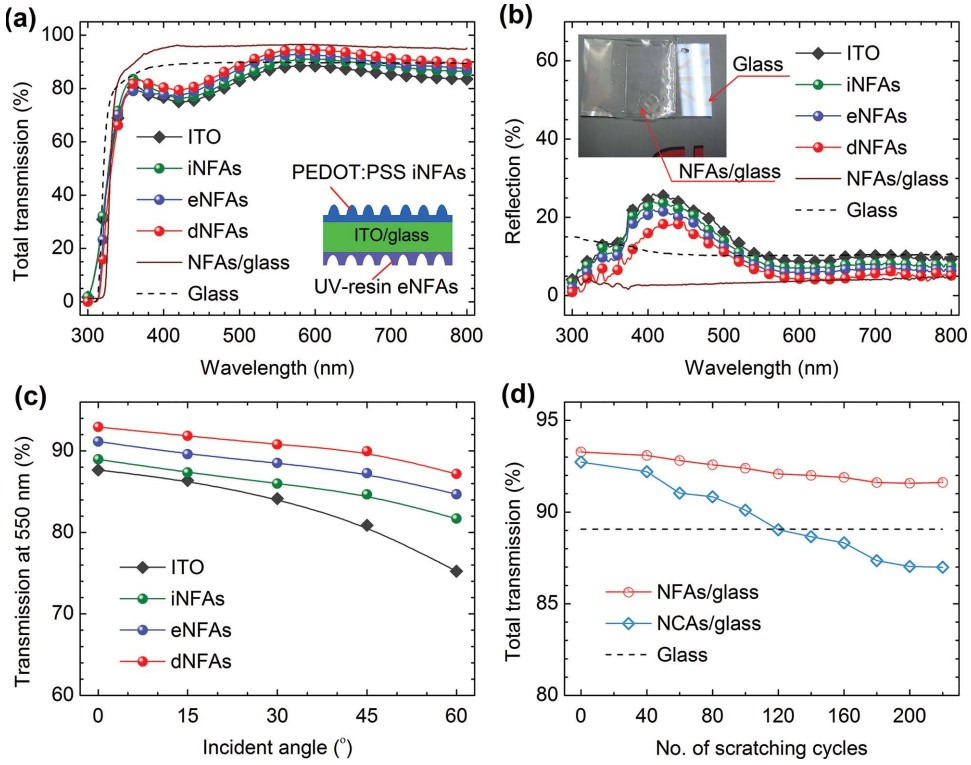

Figure 3. Optical properties and characterization against scratching of NFAs. a) Transmittance of incident light toward the ITO surface. Inset denotes the schematic of the measurement procedure. b) Reflection characteristics for incident light toward glass surface with and without NFAs. Inset depicts the ambient light reflection of glass and NFAs/glass. c) Angle-dependent transmission spectra at wavelength of 550 nm. d) Total transmittance upon the scratching test for glass substrates constructed with NFAs and NCAs.

cycles) as compared with the rapid performance degradation of NCAs (Figure 3d). In addition, as presented in Figure S4 (Supporting Information), the NFAs possessed an initial contact angle of 129°, which was almost 116° after 200 scratching cycles. However, the contact angle of NCAs decreased rapidly from 133° to 63° after the same scratching test, which was close to the value of a flat UV-resin layer.[30] As shown in the SEM images of Figure S4 (Supporting Information), the difference in the capability against scrubbing is because the cones of the NCAs can be more easily broken during the scrubbing process. Moreover, the advantageous hydrophobic character of NFAs against scratching can lead to the removal of dust particles and surface contaminants on the device (namely, the self-cleaning capability).[36,37] As a consequence, these results provide the direct experimental proof that, rather than the conventional NCAs, the NFAs are more beneficial for practical applications such as cellphones, tablet computers or any other optical surface to maximize the optical transmission with the capacity against scrubbing.

To identify the origin of this great enhancement in the transmittance characteristics using NFAs, the poynting vector **S** (energy flow) distributions for glass substrates without and with NFAs and NCAs were calculated with the excitation of a plane wave located at the semi-infinite glass. The energy flow distributions provide a quantitative understanding of the enhanced optical transmittance for the substrates with NFAs and NCAs. As presented in **Figure 4**, the energy flows traveling normally and directly into air from glass substrates with NFAs and NCAs were squeezed and funneled into air apertures, resulting in more efficient photon transmission than that from the bare glass.[38] It indicates that the origins of manipulating the trapped energy flows are identical for NFAs and NCAs with the energy primarily flowing into air through the air groove. These results match well with the measurements of optical transmittance (Figure S3, Supporting Information).

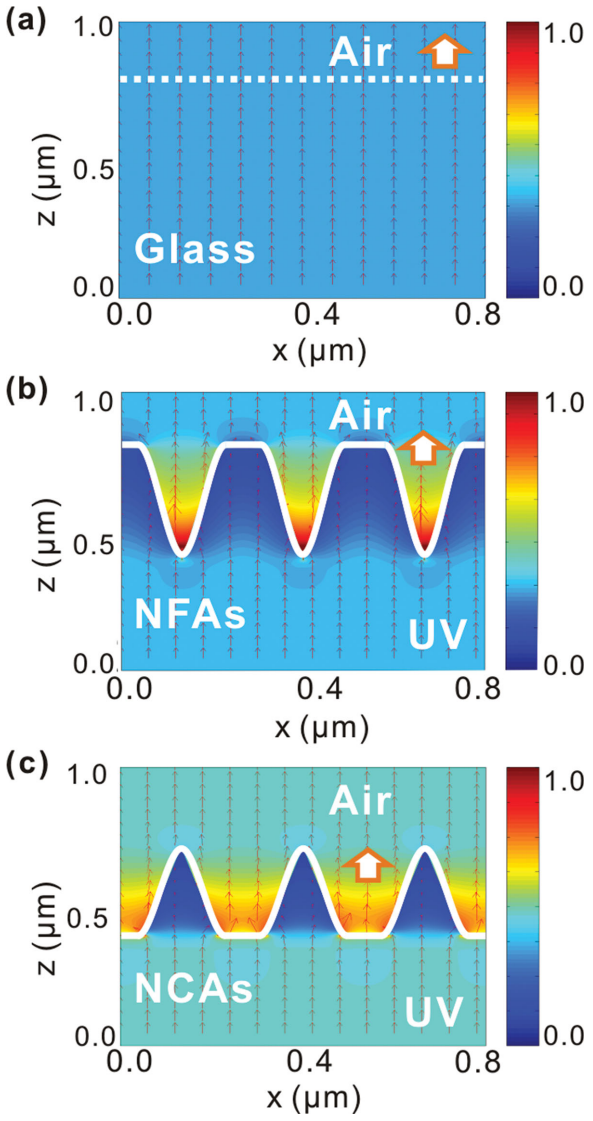

Figure 4. Calculated poynting vector **S** (energy flow) distribution excited by a plane wave (550 nm) located at the semi-infinite glass substrates: a) bare glass; b) NFAs; and c) NCAs constructed on glass surface. The NFAs and NCAs exhibit the identical period (≈250 nm), groove depth (≈200 nm), and fill factor (≈0.6). The dashed and solid lines represent the layer interface of different materials. The small arrows depict the flow direction of the energy flow.

2.3. Performance Enhancement of White OLEDs Using NFAs

The performance of white OLEDs incorporating NFAs was investigated (see the Experimental Section for the device fabrication processes). A standard white emissive layer (EML), which consisted of two complementary colors using bis(3,5-difluoro-2-(2-pyridyl)phenyl-(2-carboxypyridyl) iridium(III) (FIrpic)-doped *N,N'*-dicarbazolyl-3,5-benzene (mCP) for blue emission and Iridium (III) bis[2-metyyldibenzo (f,h) quinoxaline](acetylacetonate) [Ir(MDQ)$_2$(acac)]-doped mCP for red emission,[39] was used in all devices. The performance characteristics of white OLED with dNFAs and the control device with a flat structure are plotted in **Figure 5**. For comparison, the devices using only iNFAs and eNFAs are displayed in Figure S5 (Supporting Information). It is evident that all the devices with and without NFAs (i.e., iNFAs, eNFAs and dNFAs) exhibit almost identical current density–voltage (*J–V*) characteristics (Figure 5b), which is in good agreement with previous observations in the dark current properties of organic solar cells with the incorporation of corrugated organic layers.[22,30] Such a characteristic is different from the previous reports for OLEDs with the corrugated ITO electrodes,[27] which is because the real device areas for current transport are same for both the devices with and without NFAs. However, the luminance of the devices with NFAs was markedly increased as compared with the flat control device (Figures 5b and S5a, Supporting Information). More importantly, the normalized electroluminescence (EL) spectra of white OLEDs with and without dNFAs (Figure 5c) shows a negligible difference in the spectral profile, illustrating no specific wavelength-dependence for light extraction with NFAs over the entire visible wavelength range. The EQE and PE of various white OLEDs are plotted as a function of luminance in Figures 5d and S5 (Supporting Information). The corresponding characteristics of various devices are compared and summarized in **Table 1**. It is obvious that the EQE and PE

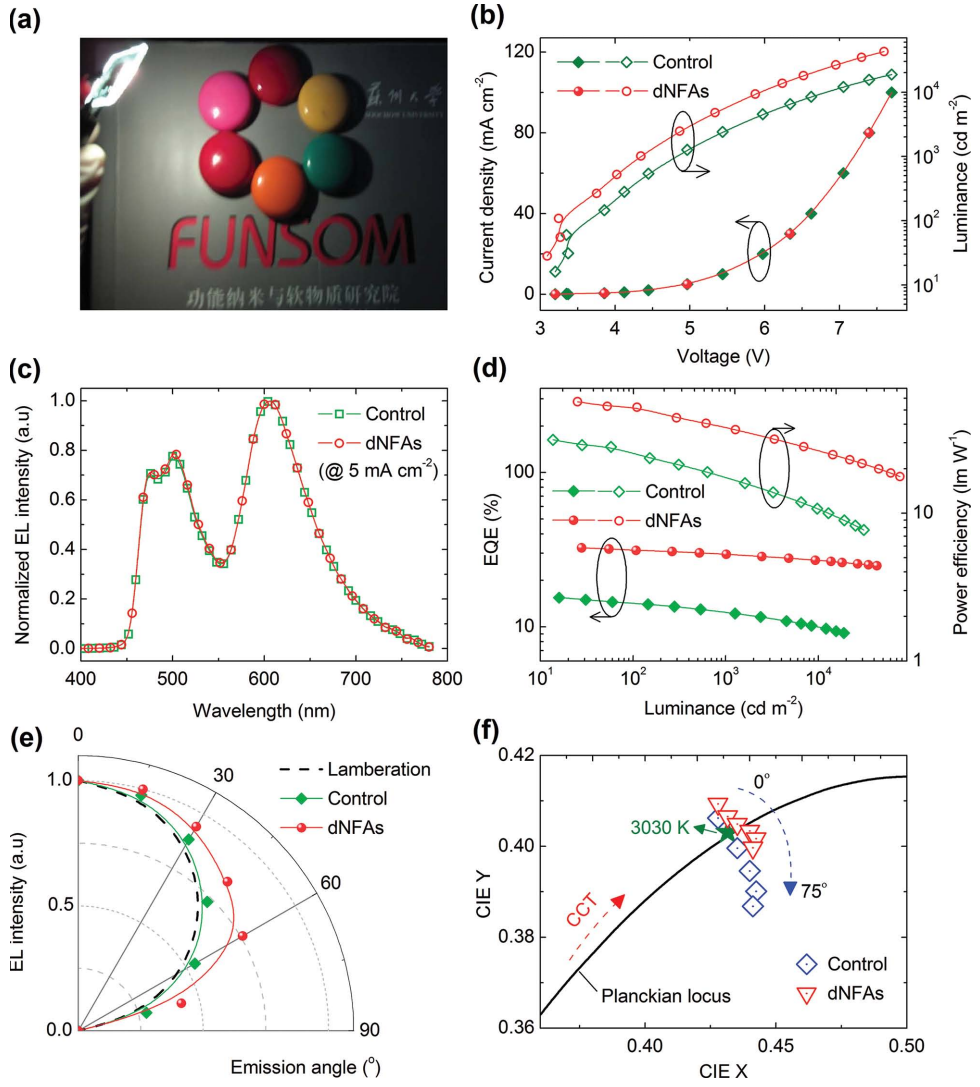

Figure 5. Performance characteristics of white OLEDs. a) Photograph of a white OLED under operation. b) Current density–luminance–voltage (*J*–*L*–*V*) characteristics of white OLEDs with and without dNFAs. c) Normalized EL spectra in the direction normal to the glass substrate at J = 5 mA cm^{-2}. d) EQE and PE as a function of luminance. e) Normalized angular dependence of light intensity for white OLEDs with and without dNFAs. The dashed line represents the ideal Lambertian emission pattern. f) CIE 1931 coordinates for white OLEDs with and without dNFAs at *J* = 5 mA cm^{-2}. The black solid line depicts the Planckian Locus. The dashed arrows indicate the decreasing direction of correlated color temperature (CCT) and the shift of color coordinates from 0° to 75°, respectively. The green star denotes the CIE coordinates of Standard Illuminant (CCT = 3030 K).

Table 1. Performance characteristics of white OLEDs without and with light extraction nanostructures. The PE and EQE are compared at their maximum values and at a luminance of 1000 cd m^{-2}. The R_{EQE} values are the enhancement ratios relative to that of the control device at a luminance of 1000 cd m^{-2}.

Device structures	EQE [1000 cd m^{-2}] [%]	R_{EQE}	PE [1000 cd m^{-2}] [lm W^{-1}]	EQE [max] [%]	PE [max] [lm W^{-1}]
Control	12.7	1	17.5	15.4	31.4
iNFAs	20.0	1.6	24.6	23.8	43.1
iNCAs	20.0	1.6	24.7	23.8	43.5
eNFAs	19.6	1.5	24.3	22.6	41.3
dNFAs	29.4	2.3	36.8	32.4	56.9

values of white OLEDs with NFAs were remarkably enhanced, and especially the use of dNFAs resulted in the largest improvement in efficiency. The white OLED with dNFAs yields an EQE of 29.4% and a PE of 36.8 lm W^{-1} at a luminance of 1000 cd m^{-2}, which are ≈2.3 and ≈2.1 times those of the control device (EQE = 12.7% and PE = 17.5 lm W^{-1}). The maximum EQE and PE of white OLED with dNFAs are increased to 32.4% and 56.9 lm W^{-1}, respectively. Apparently, the high light outcoupling with dNFAs is clearly the combined contributions of iNFAs (EQE = 20.0% and PE = 24.6 lm W^{-1}) and eNFAs (EQE = 19.6% and PE = 24.3 lm W^{-1}). This feature is in the good agreement with the increasing trend in the optical transmittance for various substrates observed in Figure 3. These results clearly prove that the implementation of NFAs into OLEDs can achieve

the efficient wavelength-independent light extraction without sacrificing the carrier transport and recombination properties. Correspondingly, a significantly enhanced contrast in white OLEDs using dNFAs can be inferred due to the high light extraction and low ambient light reflection. In addition, it is interesting to note in Table 1 that the device performance using iNFAs was nearly identical to that with iNCAs (EQE = 20.0% and PE = 24.7 lm W^{-1} at 1000 cd m^{-2}), which provided a direct evidence that NFAs can afford the identical outcoupling capability as compared with NCAs.

The angular dependence of the EL intensities of the devices with and without dNFAs is plotted in Figure 5e. Compared with the almost Lambertian emission pattern of the control device, it is noteworthy that the use of dNFAs in OLEDs causes a stronger side emission. This fact is perfectly consistent with the angular transmittance characteristics as shown in Figure 3c, indicating that dNFAs could extract the energy flow over a wider viewing angle (particularly beyond the critical angle of the glass substrate). Additionally, white OLEDs using dNFAs exhibited the nearly identical spectral shapes with increasing viewing angles, which is in contrast to the control device showing a variation of the emission spectra (Figure S6, Supporting Information). The shift in Commission Internationale d'Eclairage (CIE) coordinates (X, Y) is displayed in Figure 5d with the viewing angle varying from 0° to 75°. Compared with the large angle-dependent color shift of the control device, the emission profile of the dNFAs-based OLED is very close to the Planckian locus and Standard Illuminant A, turning out a perfect blackbody radiator of different color temperature. In addition, the fast Fourier transform pattern of the NFA on glass substrate forms the "grating vectors" in all azimuthal angles (Figure S7, Supporting Information), implying the emission from white OLEDs using dNFAs is independent on the azimuth angle due to the broadband response and quasi-omnidirectional scattering induced by dNFAs. The angular independence of white emission indicates the excellent light extraction capability of NFAs without spectral distortion, which is regarded as one of the critical requirements for full-color display and lighting applications.[40]

2.4. Optical Simulation

To gain a deeper insight into the enhancement mechanisms of white OLEDs using dNFAs, the far-field radiation distributions were calculated using the finite-difference-time-domain (FDTD) method for modeling the quasi-periodic NFAs. As shown in **Figure 6**a, the radiation profile of the control device decays dramatically away from the EML. However, the use of dNFAs can strongly modulate the far-field distribution (Figure 6b), enabling the originally trapped photons radiating into air more efficiently. Figure 6c,d compares the far-field distributions of the devices without and with dNFAs at the substrate/air interface. In contrast to the monotonical decay of the field intensity along the substrate surface for the control device (Figure 6c), the quasi-periodic NFAs strongly modulated the far-field with an almost sinusoidal grating diffraction pattern away from the center (Figure 6d). These results are highly consistent with the observation of angle-dependent emission intensities in Figure 5e, showing a stronger side emission caused by the use of NFAs.

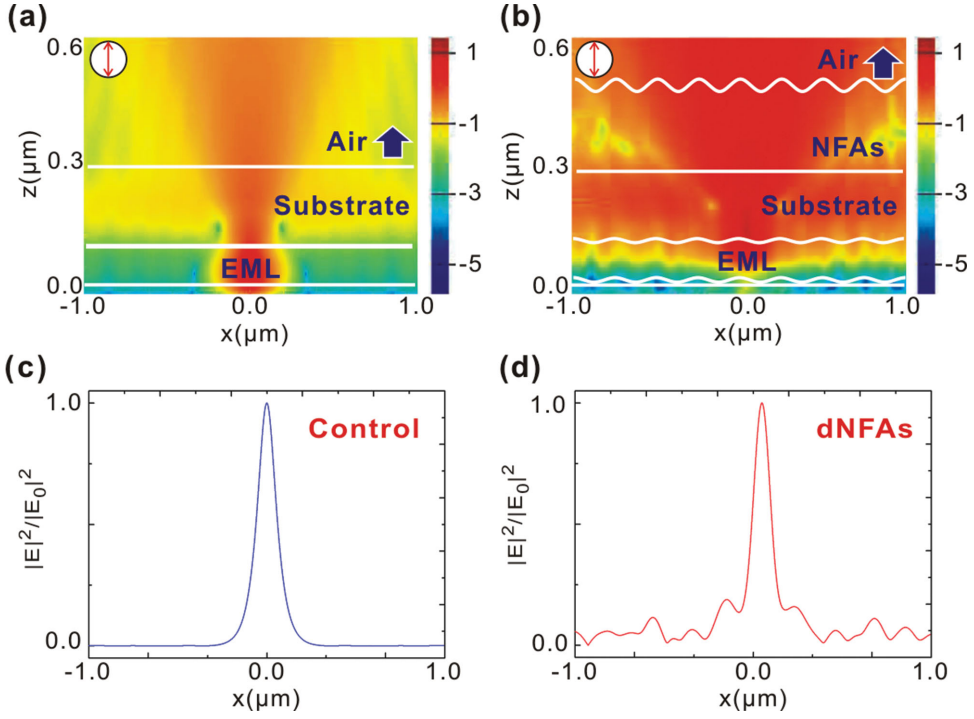

Figure 6. Calculated electric field distributions [log(E^2/E_0^2)] at 520 nm with one single perpendicular-oriented dipole, which is located in the middle of the emission layer. Far-field distributions of a) the control device and b) dNFAs-based device. Normalized 1D far-field distributions of c) the control device and d) the dNFAs-based device at the surface of the substrate/air.

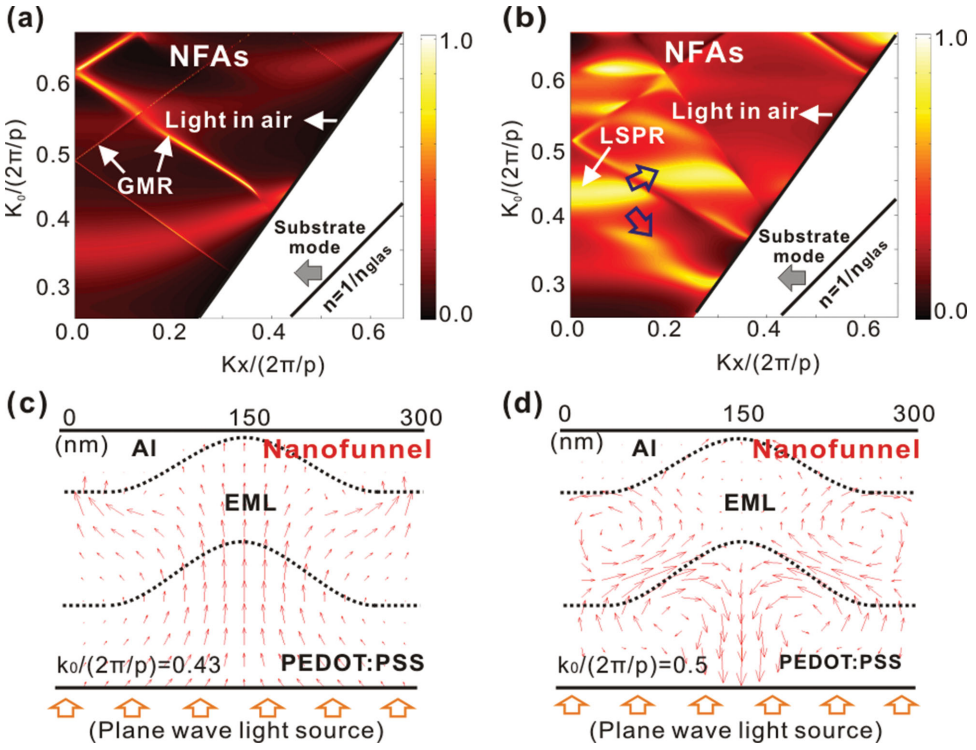

Figure 7. Simulated dispersion diagrams of a) TE and b) TM polarized light as a function of frequency and the in-plane wave vector K_x in the first Brillouin zone of the device with NFAs (fill factor = 0.6). The near-field poynting vector **S** (photon flow) distributions at c) $k_0/(2\pi/p)$ = 0.43, and d) $k_0/(2\pi/p)$ = 0.5. Red arrows depict the flow direction of the energy flow. The dashed lines represent the interfaces of different layers.

According to previous report,[41] the extraction layer constructed on glass substrate (e.g., eNFAs used here) only affects the energy dissipation for the substrate mode, while the nanostructures inside the device (e.g., iNFAs) could enable the release of the trapped energy flow in WG mode as useful radiation by manipulating various near-field optical modes. To further identify the nature of these unique near-field optical modes induced by iNFAs, the dispersion diagrams for both transverse electric (TE) and transverse magnetic (TM) polarized lights were simulated and displayed in **Figure 7** as a function of frequency and in-plane wave vector K_x in the first Brillouin zone of white OLEDs with NFAs. To compare the impacts on the manipulation of the energy flow by the counterpart topography, the dispersion diagrams of the devices with NCAs were also calculated (see Figure S8, Supporting Information). For $K_x/(2\pi/P) < k_0$, the region located above the line is named as light in air.[42] It is obvious that the devices with NFAs and NCAs show the similar dispersion diagrams. As indicated by the sharp spectral features in Figures 7 and S8 (Supporting Information), both NFAs and NCAs can enable the efficient recovery of energy flow loss from guided-mode resonance (GMR) modes of both TE and TM polarized lights, resulting in the energy flow transfer to leaky modes. This is an important factor for the efficiency enhancement in the near-field optical modulation except for the Bragg scattering. As shown in Figure 7b, the localized surface plasmonic resonance (LSPR) is excited at the corrugated organic/Al interface at a specific resonant frequency of $k_0/(2\pi/p)$ = 0.43 (at a wavelength of 580 nm), which splits into two branches due to Rayleigh-Wood anomalies (as marked by the open arrows).[43] Meanwhile, a hybrid anticross coupling between the SPPs and GMR occurs at a specific resonant frequency of $k_0/(2\pi/p)$ = 0.5 (at a wavelength of 500 nm).[44–46] Similarly, the LSPR and anticross coupling for NCAs (Figure S8, Supporting Information) are present at resonant frequencies of 0.4 and 0.5, respectively. It should be pointed out that the discrepancy in dispersion diagrams for NFAs (Figure 7) and NCAs (Figure S8, Supporting Information) is ascribed to the use of fill factor = 0.6. For an exactly complementary fill factor of 0.5, the devices with NFAs and NCAs would produce a completely identical dispersion diagram as shown in Figure S9 (Supporting Information).

The photon flux diagrams of the poynting vector **S** were calculated to unveil the origin of these unique optical modes. As shown in Figure 7c, the LSPR mode enables the Bragg scattering coupled with SPPs to radiate into leaky modes. On the contrary, anticross coupling between GMR and SPPs promotes the photon flux to propagate as an extraordinary optical vortex from the device to leaky modes eventually, which leads to the useful energy flow transfer to far-field with low propagation loss due the tight-mode confinement.[47–49] Therefore, the simulation results in Figures 6,7 are complementary to analyze the modulation behaviors of NFAs in OLEDs from the far-field and near-field viewpoints, respectively. In addition, it is noteworthy that the far-field behaviors (leaky modes) for devices with NFAs and NCAs are comparable regardless of the apparent difference in the near-field energy flow distributions. This feature matched well with the experimental results of optical transmittance and performance enhancement as discussed above.

3. Conclusion

In summary, we have demonstrated a simple and powerful method for drastically releasing the trapped energy flow in the conventional white OLEDs using a unique quasi-periodic subwavelength NFA structure via soft nanoimprinting lithography. The advantages of the NFAs used here are their abilities to 1) achieve the broadband light extraction without spectral changes and angular dependence, leading to a substantial increase in efficiency over twofold higher than a conventional device with a flat architecture as a comparison; 2) reduce the reflection of the ambient light over a broadband range, hence resulting in a significant enhancement of the OLED'scontrast; 3) tune the far-field emission pattern at a wider viewing angle with superior angular color stability; and 4) afford the enticing capacity against scrubbing and the self-cleaning feature, which are critical to the commercial viability in practical applications. Finally, the approach demonstrated here is highly versatile and fully compatible with high-throughput low-temperature roll-to-roll manufacturing on plastic flexible substrates. We therefore anticipate this method would offer a new route to the development of high-performance OLEDs for display and lighting applications.

4. Experimental Section

Device Fabrication: For the fabrication of white OLEDs, ITO-coated glass substrates were ultrasonically cleaned with detergent, acetone, ethanol, and deionized water for 20 min and subsequently dried in an oven. The 100 nm-thick PEDOT:PSS layer was spin-coated onto the ultraviolet-ozone (UVO)-treated ITO glass substrate in ambient condition, followed by a 120 °C bake on a hot plate for 20 min before the subsequent depositions of organic layers and metal electrode. After imprinting the PEDOT:PSS layer on the basis of soft nanoimprint lithography with the PDMS molds, various patterned substrates were transferred into a high-vacuum chamber with a base pressure of $< 2 \times 10^{-6}$ Torr for film deposition by thermal evaporation with a shadow mask. The film deposition for phosphorescent white emissive layers included a 45 nm-thick TAPC as the hole-transporting layer, a 10 nm-thick layer of mCP doped with 8 wt% FIrpic as the blue emissive layer, a 10 nm-thick layer of mCP doped with 8 wt% $Ir(MDQ)_2(acac)$ as the red emissive layer, a 60 nm-thick layer of 4,6-bis(3,5-di(pyridin-3-yl) phenyl)-2-methylpyrimidine (B3PYMPM) as the electron-transporting layer, and a LiF (1 nm)/Al (100 nm) bilayer cathode. The effective device area was 0.1 cm^2. To ensure consistent results, each series of white OLEDs with and without NFAs or NCAs were were simultaneously fabricated in the same batch for the spin-coating of PEDOT:PSS and the deposition of organic layers and metal electrode. The comparison of the device results were also performed from the same series of the devices.

Properties Characterization: The refractive index (n), extinction coefficient (k) and film thickness of all the layers were measured using the alpha-SE Spectroscopic Ellipsometer (J.A.Woollam Co., Inc). Optical transmission spectra were recorded by a UV–vis/near-IR spectrophotometer (Perkin Elmer Lambda 750) with an integrating sphere. Surface morphologies were characterized by AFM (Veeco MultiMode V) in tapping mode and SEM (FEI, Quanta 200FEG). Contact angle was determined by contact angle tester (DataPhysics instruments GmbH). The current density–voltage–luminance (J–V–L) characteristics and EL spectra of the devices were measured simultaneously in ambient air using a computer-controlled programmable Keithley model 2400 power source and a PhotoResearch PR655 luminance meter/spectrometer. The angle-dependent emission intensity was characterized by placing the devices on a rotating stage with one of the grooves parallel to the rotation axis.

Theoretical Simulation: The finite-difference-time-domain (FDTD) method (Lumerical FDTD Solutions 8.7.3) was used to perform the far-field radiation distribution of white OLEDs with one single perpendicular-oriented dipole located in the middle of the emission layer, using perfectly matched boundary layers in all dimensions, where the NFAs were set as the quasi-periodic structures in the range of ≈8 periods with the groove depth, period and fill factor data as determined from the AFM images. To find a rigorous solution to Maxwell's equations in the device with an outcoupling structure of NFAs and NCAs, rigorous coupled wave analysis (RCWA) was adopted to model the dispersion diagram (Rsoft DiffractMOD and corresponding codes generated in-house), and the FDTD method was used to simulate the near-field poynting vector **S** distribution (Rsoft Fullwave) with commercial RSoft 8.1 (RSoft Design Group, Inc), where the structures of NFAs and NCAs were set with one period and perfectly periodic boundary layers in all dimensions due to their short-range-order characters. The complex optical dielectric function of the nanostructured Al cathode was fitted using the Drude–Lorentz model, taking into account interband transitions and the frequency-dependent n and k values of PEDOT:PSS, ITO and UV-resin layers experimentally determined by the ellipsometer.

Supporting Information

Supporting Information is available from the Wiley Online Library or from the author.

Acknowledgements

The authors acknowledge financial support from the National Basic Research Program of China (Grant No. 2014CB932600), the National Natural Science Foundation of China (Grant Nos. 91433116 and 11474214), Jiangsu Science and Technology Department (Grant No. BK20140053), Bureau of Science and Technology of Suzhou Municipality (Grant No. ZXG201422), and the project of the Priority Academic Program Development (PAPD) of Jiangsu Higher Education Institutions.

Received: January 25, 2015
Revised: February 28, 2015
Published online: March 26, 2015

[1] J. Kido, M. kimura, K. Nagai, *Science* **1995**, *267*, 1332.
[2] B. W. D'Andrade, S. R. Forrest, *Adv. Mater.* **2004**, *16*, 1585.
[3] S. Reineke, F. Lindner, G. Schwartz, N. Seidler, K. Walzer, B. Lüssem, K. Leo, *Nature* **2009**, *459*, 234.
[4] N. Li, S. Oida, G. S. Tulevski, S. J. Han, J. B. Hannon, D. K. Sadana, T. C. Chen, *Nat. Commun.* **2013**, *4*, 2294.
[5] Q. D. Ou, L. Zhou, Y. Q. Li, S. Shen, J. D. Chen, C. Li, Q. K. Wang, S. T. Lee, J. X. Tang, *Adv. Funct. Mater.* **2014**, *24*, 7249.
[6] H. Uoyama, K. Goushi, K. Shizu, H. Nomura, C. Adachi, *Nature* **2012**, *492*, 234.
[7] Y. Sun, N. C. Giebink, H. Kanno, B. Ma, M. E. Thompson, S. R. Forrest, M., *Nature* **2006**, *440*, 908.
[8] Q. Wang, D. Ma, *Chem. Soc. Rev.* **2010**, *39*, 2387.
[9] K. Meerholz, D. C. Müller, *Adv. Funct. Mater.* **2001**, *11*, 251.
[10] G. Gu, D. Z. Garbuzov, P. E. Burrows, S. Venkatesh, S. R. Forrest, M. E. Thompson, *Opt. Lett.* **1997**, *22*, 396.
[11] B. J. Matterson, J. M. Lupton, A. F. Safonov, M. G. Salt, W. L. Barnes, I. D. Samuel, *Adv. Mater.* **2001**, *13*, 123.
[12] M. Thomschke, S. Reineke, B. Lüssem, K. Leo, *Nano Lett.* **2011**, *12*, 424.

[13] E. Wrzesniewski, S. H. Eom, W. Cao, W. T. Hammond, S. Lee, E. P. Douglas, J. Xue, *Small* **2012**, *8*, 2647.
[14] C. F. Madigan, M. H. Lu, J. C. Sturm, *Appl. Phys. Lett.* **2000**, *76*, 1650.
[15] S. Y. Hsu, M. C. Lee, K. L. Lee, P. K. Wei, *Appl. Phys. Lett.* **2008**, *9*, 013303.
[16] B. J. Matterson, J. M. Lupton, A. F. Safonov, M. G. Salt, W. L. Barnes, I. D. Samuel, *Adv. Mater.* **2001**, *13*, 123.
[17] K. Ishihara, M. Fujita, I. Matsubara, T. Asano, S. Noda, H. Ohata, N. Shimoji, *Appl. Phys. Lett.* **2007**, *90*, 111114.
[18] T. Tsutsui, M. Yahiro, H. Yokogawa, K. Kawano, M. Yokoyama, *Adv. Mater.* **2001**, *13*, 1149.
[19] Y. Sun, S. R. Forrest, *Nat. Photonics* **2008**, *2*, 483.
[20] Y. R. Do, Y. C. Kim, Y. W. Song, Y. H. Lee, *J. Appl. Phys.* **2004**, *96*, 7629.
[21] Y. C. Kim, Y. R. Do, *Opt. Express.* **2005**, *13*, 1598.
[22] L. Zhou, Q. D. Ou, J. D. Chen, S. Shen, J. X. Tang, Y. Q. Li, S. T. Lee, *Sci. Rep.* **2014**, *4*, 4040.
[23] W. Ding, Y. Wang, H. Chen, S. Y. Chou, *Adv. Funct. Mater.* **2014**, *24*, 6329.
[24] J. Hauss, T. Bocksrocker, B. Riedel, U. Geyer, U. Lemmer, M. Gerken, *Appl. Phys. Lett.* **2011**, *99*, 103303.
[25] J. Feng, T. Okamoto, S. Kawata, *Opt. Lett.* **2005**, *30*, 2302.
[26] J. W. Huh, J. W. Shin, D. H. Cho, J. Moon, C. W. Joo, S. K. Park, J. I. Lee, *Nanoscale* **2014**, *6*, 10727.
[27] W. H. Koo, S. M. Jeong, F. Araoka, K. Ishikawa, S. Nishimura, T. Toyooka, H. Takezoe, *Nat. Photonics* **2010**, *4*, 222.
[28] Lee, C. Lee, J. J. Kim, *Small* **2013**, *9*, 3858.
[29] J. Y. Kim, C. S. Choi, W. H. Kim, D. Y. Kim, D. H. Kim, K. C. Choi, *Opt. Express.* **2013**, *21*, 5424.
[30] J. D. Chen, L. Zhou, Q. D. Ou, Y. Q. Li, S. Shen, S. T. Lee, J. X. Tang, *Adv. Energy Mater.* **2014**, *4*, 1301777.
[31] L. J. Guo, *Adv. Mater.* **2007**, *19*, 495.
[32] S. Ji, J. Park, H. Lim, *Nanoscale* **2012**, *4*, 4603.
[33] K. Endo, C. Adachi, *Appl. Phys. Lett.* **2014**, *104*, 121102.
[34] J. W. Leem, S. Kim, S. H. Lee, J. A. Rogers, E. Kim, J. S. Yu, *Adv. Energy Mater.* **2014**, *3*, 1301315.
[35] J. Cai, J. Ye, S. Chen, X. Zhao, D. Zhang, S. Chen, L. Qi, *Energy Environ. Sci.* **2012**, *5*, 7575.
[36] D. H. Ko, J. R. Tumbleston, K. J. Henderson, L. E. Euliss, J. M. DeSimone, R. Lopez, E. T. Samulski, *Soft Matter* **2011**, *7*, 6404.
[37] R. Blossey, *Nat. Mater.* **2003**, *2*, 301.
[38] F. Pardo, P. Bouchon, R. Haïdar, J. L. Pelouard, *Phys. Rev. Lett.* **2011**, *10*, 093902.
[39] L. Deng, H. Shi, X. Meng, S. Chen, H. Zhou, Y. Xu, X. G. Li, L. H. Wang, B. liu Huang, W. Huang, *ACS Appl. Mater. Interfaces* **2014**, *6*, 5273.
[40] T. Schwab, S. Schubert, S. Hofmann, M. Fröbel, C. Fuchs, M. Thomschke, K. Leo, M. C. Gather, *Adv. Optical Mater.* **2013**, *1*, 707.
[41] P. A. Hobson, J. A. E. Wasey, I. Sage, W. L. Barnes, *IEEE J. Sel. Top. Quantum Electron.* **2002**, *8*, 378.
[42] L. Zhou, X. J. Jiang, Y. Q. Li, A. S. Shi, J. D. Chen, Q. D. Ou, J. X. Tang, *ACS Appl. Mater. Interfaces* **2014**, *6*, 18139.
[43] A. Christ, T. Zentgraf, J. Kuhl, S. Tikhodeev, N. Gippius, H. Giessen, *Phys. Rev. B* **2004**, *70*, 125113.
[44] H. Liu, X. Sun, Y. Pei, F. Yao, Y. Jiang, *Opt. Lett.* **2011**, *36*, 2414.
[45] E. H. Cho, H. S. Kim, J. S. Sohn, C. Y. Moon, N. C. Park, Y. P. Park, *Opt. Express.* **2010**, *18*, 27712.
[46] S. R. K. Rodriguez, S. Murai, M. A. Verschuuren, J. G. Rivas, *Phys. Rev. Lett.* **2012**, *109*, 166803.
[47] E. Sakat, G. Vincent, P. Ghenuche, N. Bardou, S. Collin, F. Pardo, R. Haïdar, *Opt. Lett.* **2011**, *36*, 3054.
[48] Y. Bian, Z. Zheng, X. Zhao, L. Liu, Y. Su, J. Xiao, T. Zhou, *IEEE J. Lightwave Technol.* **2013**, *31*, 1973.
[49] J. M. Steele, C. E. Moran, A. Lee, C. M. Aguirre, N. J. Halas, *Phys. Rev. B.* **2003**, *68*, 205103.